

Article

The Effect of Ce on the Microstructure, Superplasticity, and Mechanical Properties of Al-Mg-Si-Cu Alloy

Andrey G. Mochugovskiy ^{1,*}, Alexey S. Prosviryakov ¹, Nataliya Yu. Tabachkova ^{1,2}
and Anastasia V. Mikhaylovskaya ¹

¹ Department of Physical Metallurgy of Non-Ferrous Metals, National University of Sciences and Technology "MISIS", Leninsky Prospekt, 4, 119049 Moscow, Russia; prolex@misis.ru (A.S.P.); ntabachkova@misis.ru (N.Y.T.); mihaylovskaya@misis.ru (A.V.M.)

² Prokhorov General Physics Institute of the Russian Academy of Sciences, 8 Vavilov Str., 119991 Moscow, Russia

* Correspondence: mochugovskiy.ag@misis.ru; Tel.: +7-495-955-00-32

Abstract: The current study focuses on the influence of Ce on the superplastic behavior, microstructure, and mechanical properties of the Al-Mg-Si-Cu-Zr-Sc alloy. The multilevel microstructural analysis including light, scanning electron, and transmission electron microscopies was carried out. The simple thermomechanical treatment including the hot and cold rolling resulted in fragmentation of the eutectic originated particles of the Ce-bearing phases. The two-step annealing of the ingots provided the precipitation of the L1₂-structured Al₃(Sc,Zr) phase dispersoids with 10 nm mean size and a high number density. Due to the particle stimulated nucleation (PSN) effect caused by the particles of eutectic origin, and Zener pinning effect provided by nanoscale dispersoids of L1₂-structured phases, the studied alloy demonstrated good superplastic properties.



Citation: Mochugovskiy, A.G.; Prosviryakov, A.S.; Tabachkova, N.Y.; Mikhaylovskaya, A.V. The Effect of Ce on the Microstructure, Superplasticity, and Mechanical Properties of Al-Mg-Si-Cu Alloy. *Metals* **2022**, *12*, 512. <https://doi.org/10.3390/met12030512>

Academic Editors: Andrey Pozdniakov and Koh-ichi Sugimoto

Received: 24 February 2022

Accepted: 15 March 2022

Published: 17 March 2022

Publisher's Note: MDPI stays neutral with regard to jurisdictional claims in published maps and institutional affiliations.



Copyright: © 2022 by the authors. Licensee MDPI, Basel, Switzerland. This article is an open access article distributed under the terms and conditions of the Creative Commons Attribution (CC BY) license (<https://creativecommons.org/licenses/by/4.0/>).

Keywords: superplasticity; aluminum alloys; transition metals; dispersoids; particle-stimulated nucleation

1. Introduction

The Al-Mg-Si based (6xxx type) alloys are widely used in aircraft and machine building due to low density, good mechanical properties, and increased corrosion resistance [1–3]. The Al-Mg-Si alloys are heat treatable aluminum alloys, and the precipitation of a metastable modification of Mg₂Si phase at ageing significantly improves their strength [4–7]. Copper is an additional alloying element for commercial 6xxx type alloys that improves strengthening effect at ageing, owing to formation of the complex Q-AlCuSiMgCu phase [1,4,8,9]. The sheets of 6xxx-type alloys are promising for manufacturing of thin-walled complex-shaped parts by a superplastic forming (SPF) technology. Due to low critical cooling rate for this group of alloys, the supersaturated solid solution is formed by cooling from a solid solution treatment temperature or deformation temperature. However, the low-alloyed solid solution typically formed in 6xxx-type alloys [10] complicates grain refinement and simplifies dynamic grain growth that negatively affect the superplasticity [11]. The severe plastic deformation (SPD) results in the ultrafine structure and superplasticity in Al-Mg-Si based alloys [12–14], whereas the conventional thermomechanical treatments were not effective. Several attempts to refine grain in commercial 6061, 6013, and 6066 alloys were performed by Troeger and Stark [15,16]. The authors applied a similar approach for the Rockwell technology [17] including over-ageing with a formation of coarse Mg₂Si particles providing a particle stimulated nucleation (PSN) effect at recrystallization. The obtained materials exhibited the elongation of about 200% even at low strain rates of 0.0004 s^{−1}.

The attractive approach [18] to refine grain and provide superplasticity in aluminum alloys combines the PSN effect [17,19,20] provided by the coarse particle of eutectic origin with 0.5–2 μm size and Zener pinning effect [21–24] due to nano-scaled dispersoids. This approach was previously successfully applied for 7xxx-type [25–28], 5xxx-type [26,29–32],

2xxx-type [33] aluminum alloys doped with Ni, Fe, Er, Y. In our previous studies the effectiveness of combined PSN and Zener pinning effects for grain refinement and superplasticity was demonstrated in 6xxx-type alloy doped with Fe, Ni, and Y [34,35]. Among rare-earth metals, Cerium (Ce) is considered as a promising alloying element in aluminum alloys. The recent study demonstrated that the Ce-enriched phases fragmentize during the heat- and thermomechanical treatments and become homogeneously distributed in the Al matrix [36–38]. The positive effect of Ce on the superplasticity was demonstrated in 5xxx-type alloy [31,39]. Due to the evenly distributed particles of the Ce-bearing phases the studied alloy demonstrated a superplasticity in a strain rate range of 10^{-1} – 10^{-2} s $^{-1}$ and a temperature range of 500–540 °C. Moreover, several studies found that Ce positively affects the castability [40–45], refines of the as-cast grains and phases [46], improves wear resistance [40], creep resistance and mechanical strength of cast Al-based alloys [41,42,47,48].

The nanoscale dispersoids enhance the structure thermal stability and inhibit dynamic grain growth that favors the fine-grained structure and superplasticity [49]. Scandium (Sc) and (Zr) had proved to be the most effective dispersoid forming elements in aluminum alloys. The complex addition of Sc and Zr initiates the nucleation of core-shell Al₃(Sc,Zr) L12-structured thermally stable dispersoids with 5–10 nm size [50–52]. These dispersoids effectively inhibit grain growth, provide superplasticity [53–57], and also increase tensile strength [58–65].

The present research focuses on the influence of eutectic-forming Ce and dispersoid forming Sc and Zr on the microstructure, superplasticity, and mechanical properties of the 6xxx-type aluminum alloy.

2. Materials and Methods

For the alloys' preparation, the following pure metals and master alloys were used; (UC Rusal, Moscow, Russia) 99.99 wt.% Al, 99.95 wt.% Mg, Al-20 wt.% Ce, Al-2.5 wt.% Sc, Al-5.0 wt.% Zr, Al-59.5 wt.% Cu, Al-12.0 wt.% Si. The master alloys were added to the melt first after the aluminum melt reached the required temperature. The alloys' compositions are presented in Table 1. The melting process was carried out in an inductive furnace (Interselt, Saint-Petersburg, Russia) using graphite-fireclay crucibles (Lugaabrasiv, Luga, Russia). The temperature of the melt before casting was 790 ± 20 °C. The chromel-alumel thermocouple was used to control the temperature. The casting was performed to a water-cooled copper mold with internal dimensions of $100 \times 40 \times 20$ mm. The cooling rate during the casting procedure was about 15 K/s. The as cast samples were subjected to a two-step homogenization with the first step at 350 °C for 8 h and the second step at 480 °C for 3 h. The heat treatment was performed in a Nabertherm N30/65A furnace with air-forced convection (Nabertherm, Lilienthal, Germany). The thermomechanical treatment included hot and subsequent cold rolling (Rolling mill V-3P, GMT, Saint-Petersburg, Russia) with 75 and 80% thickness reduction, respectively. The hot rolling temperature was 420 ± 20 °C. The rolls diameter was 250 mm, the rolling speed was 10 m/s. The strain rate was 15 s $^{-1}$.

Table 1. Chemical compositions of the studied alloys (wt.%).

Alloy	Mg	Si	Cu	Ce	Sc	Zr	Al
0Ce	1.2	0.7	1.0	-	0.10	0.2	bal.
2Ce	1.2	0.7	1.0	2.0	0.10	0.2	bal.
4Ce	1.2	0.7	1.0	4.0	0.10	0.2	bal.

The X-ray diffraction (XRD) analysis was carried out to analyze the phase composition of the studied materials. The powder of the studied alloys was exposed under Cu-K α radiation using a Bruker D8 Advanced diffractometer (Bruker Corporation, Billerica, MA, USA). The peaks identification was carried out using the Powder Diffraction Data (PDF-MaintEx library v. 9.0.133) database using a DIFFRAC.EVA software (v.12.0 rev.0, Bruker AXS GmbH, Karlsruhe, Germany).

The microstructural evolution and chemical composition of the studied alloys were studied using a Tescan-VEGA3 LMH scanning electron microscope (SEM) (Tescan Brno s.r.o., Kohoutovice, Czech Republic) equipped with an energy dispersive X-ray spectrometer (EDS) X-MAX80, and an electron backscatter diffraction (EBSD) detector HKL NordlysMax (Oxford Instruments plc, Abingdon, UK). The samples were grinded with SiC papers and further polished with OP-S silica colloidal suspension using a Struers LaboPoll-5 polishing machine (Struers APS, Ballerup, Denmark). The EBSD maps were exposed from an area of $150 \times 150 \mu\text{m}^2$ with a step size of $0.3 \mu\text{m}$.

The JEOL JEM 2100 microscope (JEOL, Tokyo, Japan) equipped with an EDS analyzer (Oxford Instruments plc, Abingdon, UK) was used for transmission electron microscopy (TEM) analysis. The microscope operating voltage was 200 kV. The disc-shaped specimens with 3 mm diameter and 0.2 mm thickness were used for probe preparation. The specimens were subjected to a twin-jet polishing at a voltage of 21 V and a temperature of $-(20-25)^\circ\text{C}$ using a 30% HNO_3 solution in methanol and a Struers TenuPol-5 machine (Struers APS, Ballerup, Denmark).

The grain structure of samples before the start of the superplastic deformation was analyzed with an optical microscopy (OM) in a polarized light mode. The Zeiss Axiovert 200 M optical microscope (Carl Zeiss, Oberkochen, Germany) was used. The samples for OM were polished with OP-S suspension (Struers APS, Ballerup, Denmark) and further anodized with Barker's reagent at a temperature of 0°C and a voltage of 16 V.

The Walter Bai LFM-100 machine (Walter + Bai AG, Löhningen, Switzerland) was used to study the elevated temperature deformation behavior of the studied alloys following ASTM-E2448-11 standard. The uniaxial tensile tests were performed in a temperature range of $440-520^\circ\text{C}$ and a constant strain rate range of $2 \times 10^{-3}-5 \times 10^{-2} \text{ s}^{-1}$. The machine crosshead velocity is increased according to the Equation (1) to an accuracy of $\pm 1\%$ to maintain a constant true strain rate until a predetermined strain value is reached or until fracture.

$$V = \dot{\epsilon}[L_0(1 + e)] \quad (1)$$

where V is crosshead velocity,

L_0 is initial gauge length,

e is true strain.

The Dion-Pro+ software (v.4.8, Walter + bai company, Löhningen, Switzerland) was used to control the crosshead movement during the test. The standard samples with the gauge length $L_0 = 5.65\sqrt{F_0}$, where F_0 is the cross sectional area, and the initial gauge section dimensions of $6 \times 1 \times 14 \text{ mm}^3$ were used for the tensile tests. Three samples were analyzed per each testing regime.

The derived "m" value was determined according to the ASTM-E2448-11 (American Society for Testing and Materials) standard using a step test, in which the true strain rate was periodically stepped to 20% above nominal, then back to nominal, starting at a true strain of 0.15 and stepping up and down every 0.1 strain.

The room temperature mechanical properties were measured according to ASTM E8/E8M standard using a Zwick Z250 universal testing machine (Zwick/Roell, Ulm, Germany). Three samples per state were analyzed.

3. Results and Discussion

3.1. Microstructural and Phase Composition Analyses

The XRD analysis was performed to reveal the phase composition for the studied alloys in the homogenized state (Figure 1). According to the obtained spectrums, the (Al), Al_3CuCe , $\text{Al}_{11}\text{Ce}_3$, $\text{Al}_{12}\text{Ce}_{10}\text{Si}_8$, and Mg_2Si phases solidified in the alloys studied.

The aluminum based solid solution and eutectic originated phases at the periphery of dendrite cells were observed after the homogenization annealing (Figure 2). According to the SEM-EDS analysis, the phase with dark contrast was enriched with Mg and Si and corresponded to Mg_2Si phase in the 0Ce (Ce-free) alloy (Figure 2a). The Mg_2Si phase

volume fraction was $3.1 \pm 0.3\%$. A negligible fraction of the Sc and Si bearing phase was also found. The solidification of the AlSc_2Si_2 phase [66,67] is suggested.

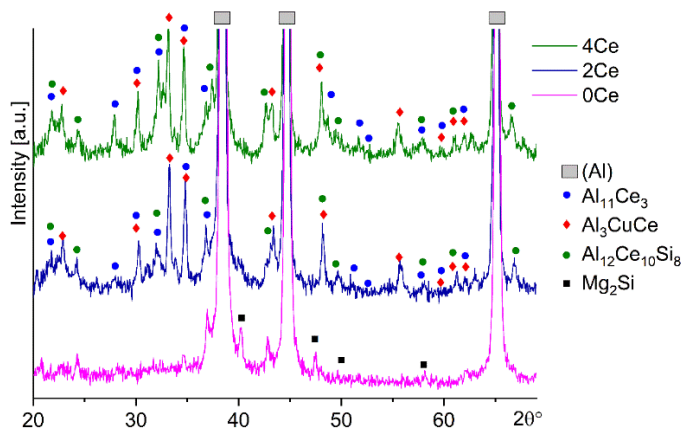


Figure 1. The XRD data for the studied alloys after a two-step homogenization annealing.

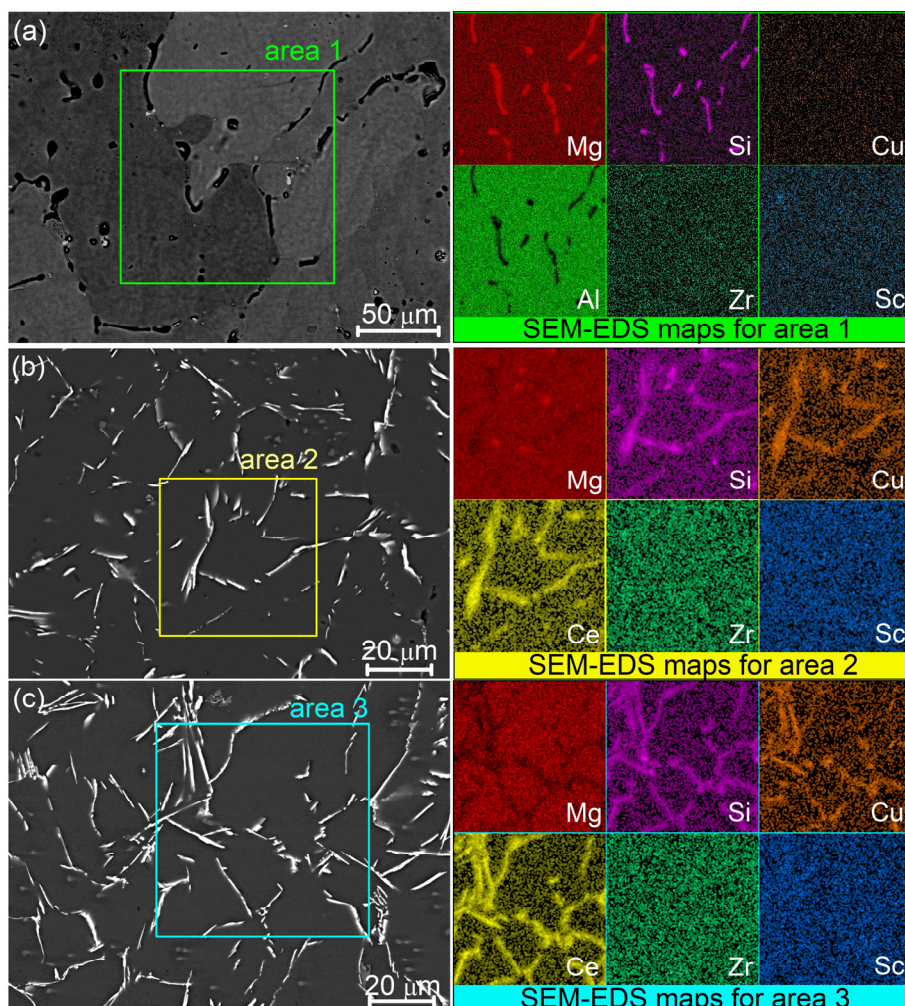


Figure 2. SEM-BSE micrographs and corresponded SEM-EDS maps for (a) 0Ce, (b) 2Ce, and (c) 4Ce alloys after a two-step homogenization.

The dark particles enriched with Mg and Si and attributed with the Mg_2Si phase were also observed in the Ce-bearing alloys. The Mg_2Si -phase with volume fraction was 0.6 ± 0.1 for the 2Ce alloy, and it was noticeably smaller at 0.2 ± 0.1 for the 4Ce alloy (Figure 2b,c).

In the Ce-bearing alloys, a high fraction of bright contrast eutectic phases enriched with the Si, Cu, and Ce were observed (Figure 2b,c). The eutectic phases particles predominately exhibited a needle-shaped morphology. The volume fraction of the particles was $5.5 \pm 0.4\%$ and $10.5 \pm 0.6\%$ for the 2Ce and 4Ce alloys, respectively.

The TEM-EDS analysis of the eutectic originated particles in the 4Ce alloy revealed the Ce, Cu, Al, Si, Zr, and Sc elements (Figure 3). The concentrations of the Sc and Zr in the particles (Spectrum 1 and 2 in Figure 3a and Table 2) were similar to that in the solid solution (Spectrum 3 in Figure 3a and Table 2). The obtained spectrums suggested two types of Ce-rich phases with low Cu and high Si (spectrum 1 in Figure 3a) and with high Cu and low Si (Spectrum 2 in Figure 3a).

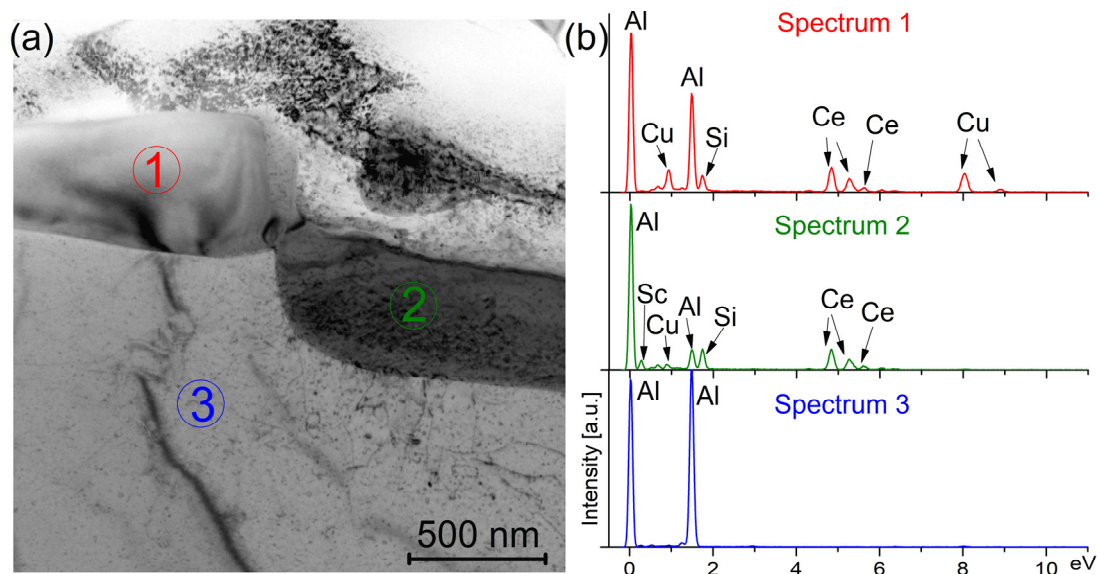


Figure 3. (a) TEM micrographs of the eutectic originated particles in the as-homogenized 4Ce alloy; (b) the TEM-EDS spectrums for the areas 1–3 marked-up with circles in (a).

Table 2. Elemental composition (at.%) corresponded to the spectrums 1–3 in Figure 3b.

	Al	Mg	Si	Cu	Ce	Sc	Zr
Spectrum 1	43.40	0.54	7.90	26.40	21.40	0.10	0.02
Spectrum 2	43.50	0.17	24.20	2.50	29.40	0.18	0.11
Spectrum 3	97.72	1.60	0.03	0.50	-	0.12	0.15

The comparative analysis of the XRD, SEM, and TEM results suggested the presence of several Ce-bearing phases in the studied alloys. The Al_3CuCe , $\text{Al}_{11}\text{Ce}_3$, $\text{Al}_{12}\text{Ce}_{10}\text{Si}_8$ were observed by XRD in both 2Ce and 4Ce alloys. The increase in Ce content provide a decrease in the Mg_2Si -phase volume fraction that was explained by a formation of Si- and Ce-bearing phases. It should be noted that the increase in Ce content from 2 to 4% resulted in an increase in the heights of the XRD-peaks corresponded to the $\text{Al}_{11}\text{Ce}_3$ -phase, therefore, its fraction can increase. The SEM-EDS and TEM-EDS data demonstrated that the Ce-bearing phase was also enriched with Cu and Si. The TEM-EDS analysis allowed distinguishing two-types of Ce-bearing phases with high Cu/low Si content and low Cu/high Si content. We suggested that the Si partially dissolved in the Al_3CuCe , whereas the Cu dissolved in the $\text{Al}_{12}\text{Ce}_{10}\text{Si}_8$ phases and both elements dissolved in the $\text{Al}_{11}\text{Ce}_3$ phase without the changes of the phases' lattice structure. As an example we can provide the following papers [67–69] that revealed the dissolution of Si in $\text{Al}_3(\text{Sc},\text{Zr})$ phase or dissolution of Cr and Fe in the Al_6Mn phase.

The mechanical treatment provided the fragmentation of the eutectic originated particles that were uniformly distributed in the matrix (Figure 4). The Mg_2Si particles in

the 0Ce alloy exhibited a mean size of $1.8 \pm 0.1 \mu\text{m}$ and a volume fraction of $3.0 \pm 0.1\%$ (Figure 4a). After sheet processing, the Mg_2Si phase particles size was $1.3\text{--}1.8 \mu\text{m}$ and their volume fraction was $0.5 \pm 0.1\%$ and $0.2 \pm 0.1\%$ for the 2Ce and 4Ce alloys, respectively. The Ce-bearing particles exhibited a mean size of $1.9 \pm 0.1 \mu\text{m}$ and $1.4 \pm 0.1 \mu\text{m}$ for the 2Ce and 4Ce alloys, respectively (Figure 4b,c). The particles size varied in a range of 0.4 to $5.6 \mu\text{m}$. The particles size distribution histograms demonstrated near-normal size distribution. The volume fraction of the particles was $5.5 \pm 0.4\%$ and $10.5 \pm 0.6\%$ for the 2Ce and 4Ce alloys, respectively.

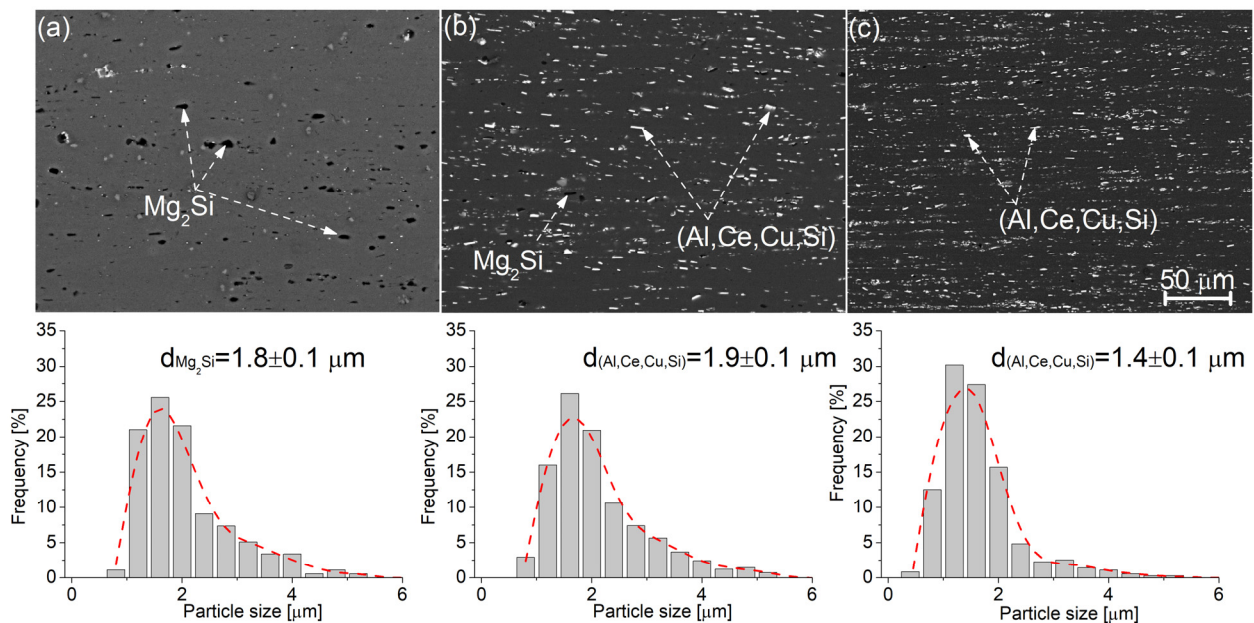


Figure 4. SEM-BSE images of the studied alloys in the as-cold rolled state and corresponded particle size distribution histograms.

The TEM study of the alloys revealed a high number density of dispersoids with a mean size of $10 \pm 1 \text{ nm}$ (Figure 5). The selected area electron diffraction (SAED) of the analyzed area demonstrated the reflection pattern of Al [110] zone axis and ordered superlattice reflections corresponded to the L_{12} -phase (insert in Figure 5b). The high-resolution image revealed the coherency of the dispersoids and Al matrix (Figure 5c) that agrees with earlier studies performed in Sc- and Zr-bearing Al-Mg-Si-based alloys [35,70]. The fast Fourier transform (FFT) of the high-resolution image also confirmed the L_{12} structural type of the precipitates (insert in Figure 5c). The L_{12} precipitate's size and structure were the same for the alloys studied.

To analyze the grain structure of the studied alloys before the start of superplastic deformation, the sheets were annealed in a temperature range of $460\text{--}500 \text{ }^\circ\text{C}$ for 20 min (Figure 6). In studied conditions the sheets exhibited non-recrystallized banded grain structure. The high number density and small size of L_{12} dispersoids provided a strong dislocation pinning effect and inhibited recrystallization during heating. Therefore, the thermomechanical treated samples demonstrated a non-recrystallized structure before the start of the superplastic deformation.

3.2. The Superplastic Deformation Behavior

The superplastic behavior for the studied alloys was analyzed in a temperature range of $460\text{--}500 \text{ }^\circ\text{C}$ and a constant strain rate range of $2 \times 10^{-3}\text{--}5 \times 10^{-2} \text{ s}^{-1}$. The obtained true stress vs true strain curves are presented in Figure 7. The flow stress decreased with a decrease in strain rate and increase in temperature. The increase in Ce content resulted in a decrease in stress values and increase in elongation-to-failure. The strain hardening effect was observed at low strains and a strain softening occurred at larger

strain values. A similar behavior was observed for various superplastic alloys with initially non-recrystallized grain structure [71,72]. Strain hardening is associated to the grain growth effect [11,18]. In the studied alloys, the strain hardening effect was observed at low strains owing to the increased dislocation density. The strain softening is attributed with dynamic recrystallization (DRX). Increase in the dislocation density to a critical level is required to start the dynamic recrystallization (DRX) [73]. When above the critical point, the DRX starts and helps to form a fine-grained structure. Due to a simplifying of the DRX, the strain softening effect is weakened with an increase in the deformation temperature and the Ce content in the alloys.

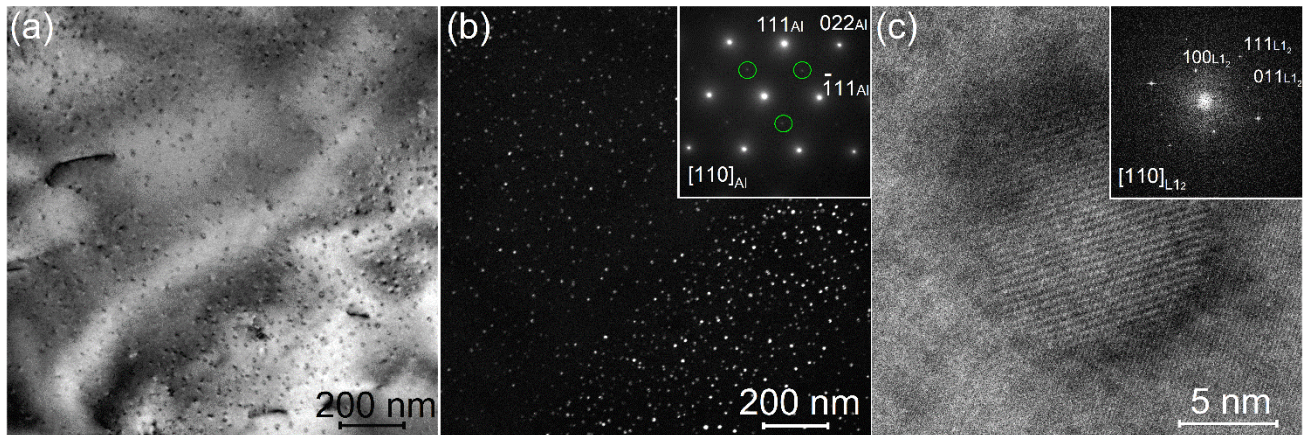


Figure 5. TEM micrographs for the 4C alloy; (a) bright field; (b) dark field; (c) high-resolution image of dispersoid; insert in (b) is corresponding SAED and insert in (c) is corresponding FFT.

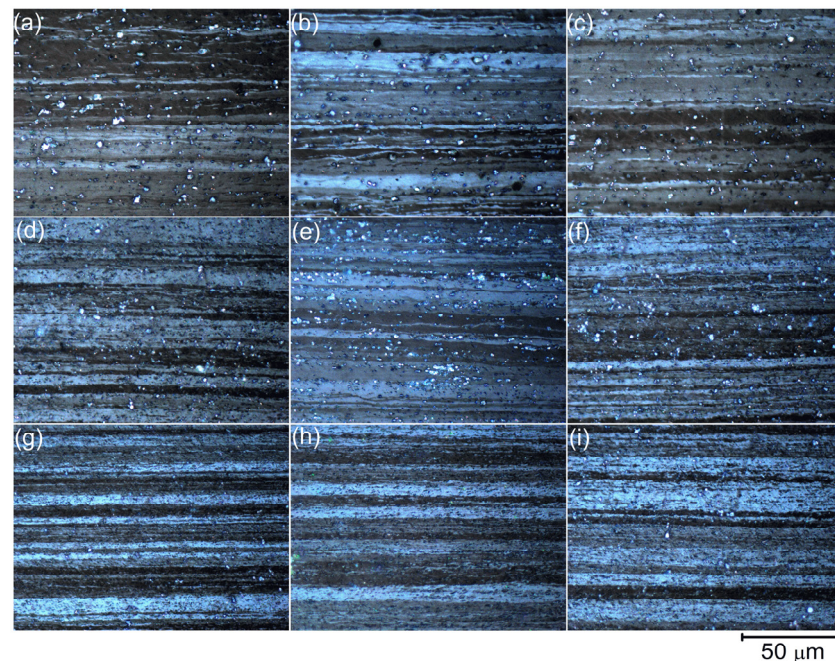


Figure 6. Grain structure of the (a–c) 0Ce, (d–f) 2Ce, (g–i) 4Ce alloy sheets after 20 min annealing at (a,d,g) 460 °C, (b,e,h) 480 °C, (c,f,i) 500 °C.

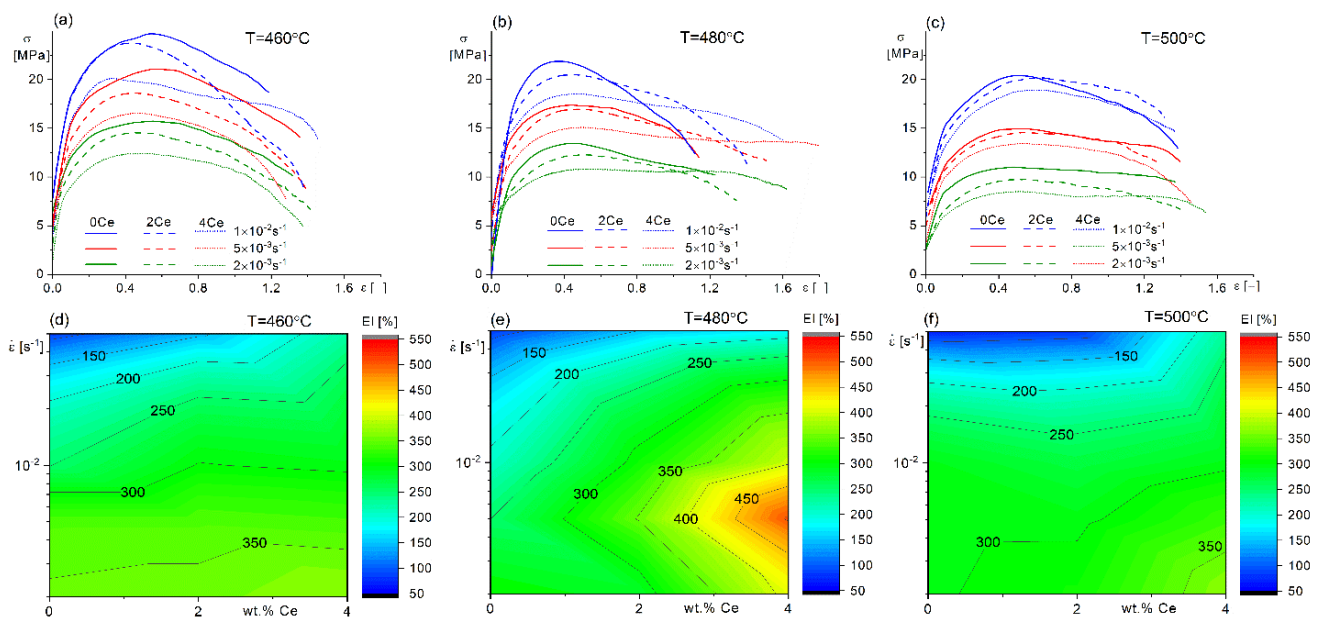


Figure 7. (a–c) True stress vs true strain curves for 0Ce, 2Ce, and 4Ce alloys for a constant strain rates of 2×10^{-3} , 5×10^{-3} , and $1 \times 10^{-2} \text{ s}^{-1}$; (d–f) elongation-to-failure diagrams as a function of strain rate and Ce content in the alloys for the deformation temperatures of (a,d) 460, (b,e) 480, (c,f) 500 °C.

The maximum elongation-to-failure of 400–500% was observed at 480 °C for the 4Ce alloy in a strain rate range of 2×10^{-3} – $1 \times 10^{-2} \text{ s}^{-1}$. A better superplastic behavior of the 4Ce alloy was the result of a higher volume fraction of the coarse particles that provided the PSN effect. As a result, the coarse particles simplified the DRX and this led to a grain refinement during the deformation. At a low deformation temperature of 460 °C and elevated temperature of 500 °C, an elongation to failure increased less significantly with an increase in the fraction of coarse particles, however the maximum value of $350 \pm 10\%$ was also observed for the 4Ce alloy.

A strain-induced change of the strain rate sensitivity m -coefficient was analyzed for the studied alloys at 480 °C that provided the maximum elongation to failure (Figure 8). For the nominal strain rate values of $5 \times 10^{-3} \text{ s}^{-1}$ and $1 \times 10^{-2} \text{ s}^{-1}$, the calculated values of the m -coefficient varied from 0.25 to 0.43 for the 0Ce alloy and from 0.28 to 0.45 for the 2Ce and 4Ce alloys. An increase in the m -value was observed at small strains, which agreed with DRX behavior. A similar strain induced change to the m -value was found for alloys with initial non-recrystallized grain structure in Ref. [11].

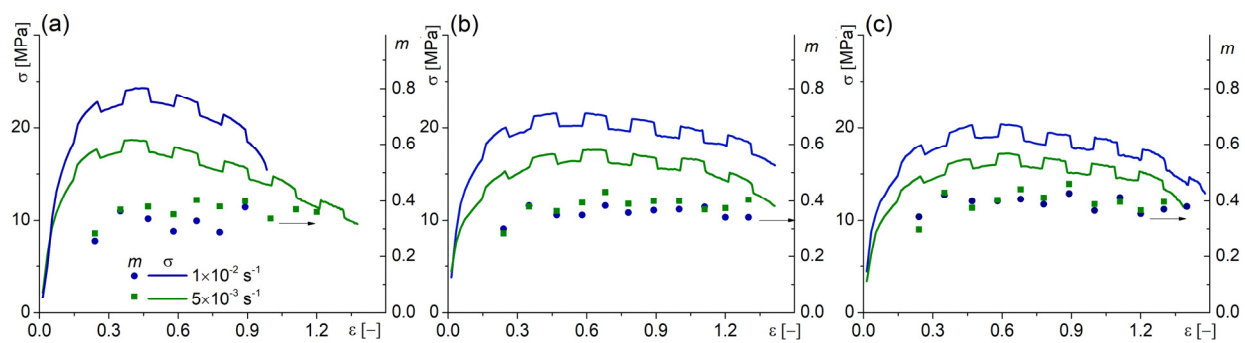


Figure 8. Strain dependence of the stress and m -value during the step test with periodically stepped true strain rate to 20% above nominal of $5 \times 10^{-3} \text{ s}^{-1}$ and $1 \times 10^{-2} \text{ s}^{-1}$, then back to nominal for (a) 0Ce, (b) 2Ce, and (c) 4Ce alloys at 480 °C.

According to the Equation (2) [74] the flow stress at superplastic deformation (σ) depends on the deformation temperature (T), the strain rate ($\dot{\epsilon}$), and the strain (ϵ),

$$\sigma = f(T, \dot{\epsilon}, \epsilon) \quad (2)$$

The Zener–Holloman parameter (Z) is used to describe the hot deformation behavior (Equations (3) and (4)) [75,76].

$$Z = \dot{\epsilon} \exp\left(\frac{-Q}{RT}\right) \quad (3)$$

$$\dot{\epsilon} = Af(\sigma) \exp\left(\frac{-Q}{RT}\right) = \begin{cases} A_1 \sigma^{n_1} \left(\exp\left(\frac{-Q_1}{RT}\right)\right) \\ A_2 \exp(\beta\sigma) \exp\left(\frac{-Q_2}{RT}\right) \\ A_3 [\sinh(\alpha\sigma)]^{n_2} \left(\exp\left(\frac{-Q_3}{RT}\right)\right) \end{cases} \quad (4)$$

where $A_{1,2,3}$, α ($\alpha = \beta/n_1$), β , n_1 , n_2 are the material constants that depend on the effective strain, $Q_{1,2,3}$ are the effective activation energy of superplastic deformation, kJ/mol, T is the absolute temperature, K , R is the universal gas constant, 8.314 J/(mol·K). A mean strain rate sensitivity m -coefficient is calculated as $1/n_1$.

The sigmoidal-type equation covers the deformation behavior well with a wide strain rate and temperature ranges, and therefore, this model is often applied to analyze the activation parameters of the superplastic deformation [77,78]. The calculated mean values of the m -coefficient for the studied alloy in a temperature range of 460–500 °C and strain rate range of 2×10^{-3} – 1×10^{-2} s $^{-1}$ was 0.34–0.40 that excess the threshold of superplastic deformation (Table 3). The experimental m -values determined via a step test at the optimal temperature of 480 °C and strain rate of 5×10^{-3} s $^{-1}$ was 0.39–0.42 at a strain of 0.41. The $m = 0.5$ is associated with the grain boundary sliding (GBS) as the main superplastic deformation mechanism [74]. Lower m values for the alloys studied can be explained by partially recrystallized grain structure and less developed GBS.

Table 3. The material parameters and the effective activation energy of the superplastic deformation values for the Equation (4) calculated for a true strain of 0.41 (50%).

Strain [%]	Q_1 [kJ/mol]	n_1/m	$\ln A_1$	Q_2 [kJ/mol]	β [MPa $^{-1}$]	$\ln A_2$	Q_3 [kJ/mol]	n_2	$\ln A_3$
0Ce	98 ± 4	2.89/0.34	2.1	100 ± 5	0.16	7.8	100 ± 7	2.21	10.3
2Ce	92 ± 3	2.72/0.37	1.9	98 ± 7	0.17	7.4	96 ± 7	2.06	9.5
4Ce	67 ± 8	2.46/0.40	1.1	70 ± 10	0.18	3.1	69 ± 8	1.87	5.2

The effective activation energy of the superplastic deformation Q_3 decreased from 100 to 69 kJ/mol with an increase in the Ce content from 0 to 4%. Considering error bars, the calculated values of the activation energy were close to the activation energy of the grain boundary self-diffusion in aluminum ($Q = 84$ – 86 kJ/mol [74,79,80]). Similar effective activation energy values of the superplastic deformation were observed for various aluminum-based alloys in Refs. [53,81].

The decrease in Q values with increasing Ce was the result of an intensification in dynamic recrystallization. The increase in Ce provides a stronger PSN effect and refines grain. As a result, the fraction of high-angle grain boundaries increases, and the grain boundary diffusion intensifies. Both the calculated effective activation energy and m -coefficient values speak for the grain boundary sliding is a predominant deformation mechanism in studied alloys.

The grain/sub-grain structure was studied with EBSD technique after 200% of the superplastic deformation at 480 °C and 1×10^{-2} s $^{-1}$ (Figure 9). An increase fraction of low angle grain boundaries was observed in the alloys studied, therefore, the microstructure was partially non-recrystallized, even after the superplastic deformation. The misorientation angle distribution transformed from the low-angle grain boundaries domination to a high angle one with an increase in Ce content and the related increase fraction of the coarse

particles. The Ce-bearing alloys demonstrated finer grain structure. The 0Ce alloy exhibited the grain and sub-grain sizes of $4.3 \pm 0.2 \mu\text{m}$ and $3.9 \pm 0.1 \mu\text{m}$, respectively (Figure 9a). The Ce-bearing alloys demonstrated smaller grain and sub-grain sizes. The grain/sub-grain sizes were $3.8 \pm 0.3 \mu\text{m}/3.3 \pm 0.1 \mu\text{m}$ for 2Ce alloy and $3.4 \pm 0.2 \mu\text{m}/3.2 \pm 0.1 \mu\text{m}$ for 4Ce alloy, respectively (Figure 9b,c).

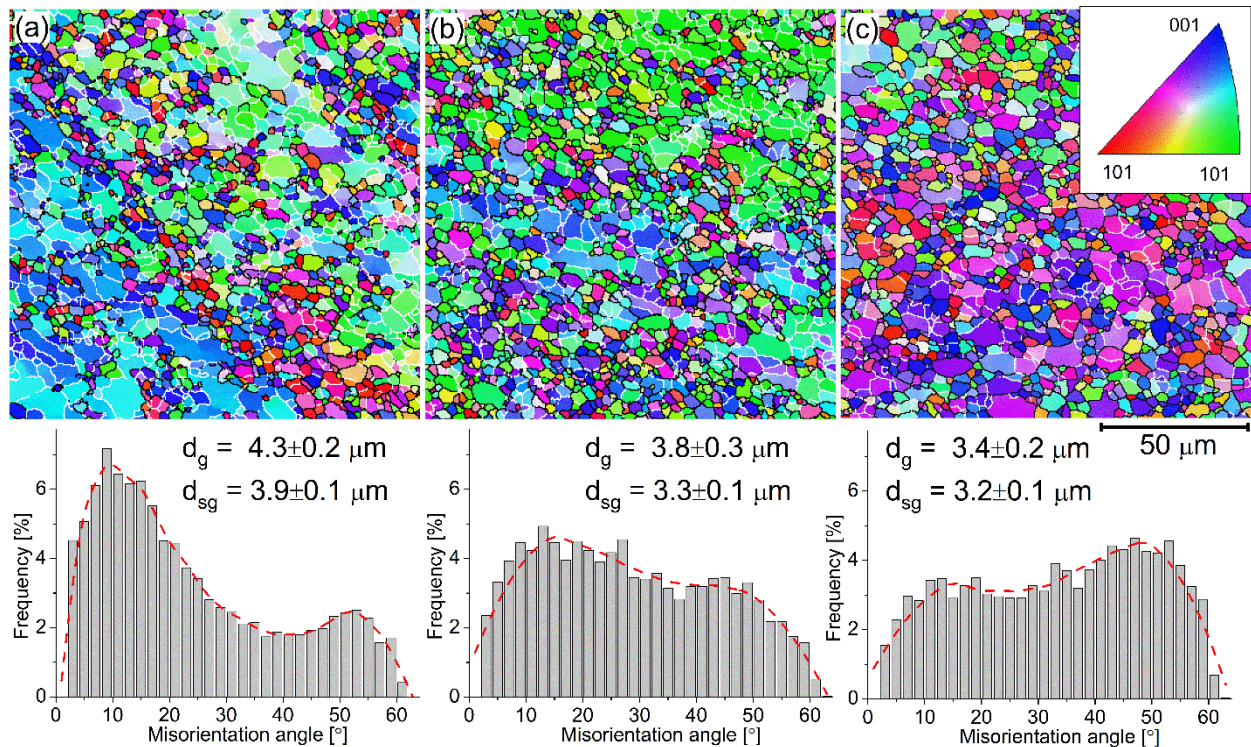


Figure 9. EBSD-IPF grain boundary maps and corresponded misorientation angle distribution histograms for the (a) 0Ce, (b) 2Ce, and (c) 4Ce alloys after 200% of superplastic deformation at $480 \text{ }^\circ\text{C}$ and $1 \times 10^{-2} \text{ s}^{-1}$ strain rate.

3.3. Room Temperature Mechanical Properties

The mechanical properties at room temperature were analyzed using uniaxial tensile test and hardness measurement (Table 4). The thermomechanical-treated samples were preliminarily subjected to a solid solution treatment (SST) at $520 \text{ }^\circ\text{C}$ for 20 min and subsequently aged at $180 \text{ }^\circ\text{C}$ for 8 h. After SST and water cooling, the strength characteristics of the studied alloys were not significantly different. Due to an increase in the volume fraction of Ce-bearing particles, the hardness changed from 65 ± 2 to 72 ± 3 HV and yield strength (YS) from 140 ± 1 to 160 ± 1 MPa with an increase in Ce content from 0 to 4%. The subsequent ageing results in a noticeable increase in the strength characteristics of the Ce-free alloy. The hardness, YS and ultimate tensile strength (UTS) values for the 0Ce alloy were 126 ± 3 HV, 367 ± 1 MPa and 420 ± 4 MPa, respectively, that correlate well with data in Ref. [70]. The strengthening effect at aging of the Al-Mg-Si-(Cu) alloys is due to the precipitation of β'' , β' , Q' metastable phases [4,8,9]. The strength characteristic for the 0Ce alloy were approximately 50 MPa higher than that for the conventional AA6013 T6-treated sheets [82]. The increase in strength can be explained by a strengthening effect of the L_{12} phase precipitates. The L_{12} dispersoids can increase the alloy's strength following the dislocation shearing and Orowan dislocation bypass looping mechanisms. The Al_3Zr L_{12} -structured dispersoids smaller than 5.6 nm in size [79] are sheared by dislocation,

whereas coarser precipitates induce Orowan strengthening that can be estimated following the Equation (5a):

$$\Delta\sigma_{or} = \frac{M \cdot 0.4 \cdot Gb}{\pi \sqrt{(1-\nu)}} \cdot \frac{\ln\left(\frac{2\bar{R}}{r_0}\right)}{\lambda}, \quad (5a)$$

where $\nu = 0.345$ is the Poisson ratio, $M \sim 3.0$ is the Taylor factor, $G = 26\text{GPa}$ is the shear modulus, $b = 0.286\text{ nm}$ is the Burgers vector, $\bar{R} = \pi \cdot D_s / 8$ and D_s are the mean precipitate radius and the diameter, $r_0 = 1.5b$, λ is the interparticle space (nm):

$$\lambda = 0.5D_s \cdot \left(\sqrt{\frac{2\pi}{3\varphi}} - \frac{\pi}{4} \right), \quad (5b)$$

where φ is the volume fraction of precipitates.

Table 4. Mechanical properties of the thermomechanical-treated samples after solid solution treatment and artificial aging (standard deviation are presented as an error bar).

Alloy	SST at 520 °C (20 min)				SST and Aging at 180 °C for 8 h			
	HV	YS [MPa]	UTS [MPa]	EI [%]	HV	YS [MPa]	UTS [MPa]	EI [%]
0Ce	65 ± 2	140 ± 1	256 ± 3	20 ± 2	126 ± 3	367 ± 1	420 ± 4	9 ± 1
2Ce	68 ± 3	150 ± 2	255 ± 5	15 ± 1	102 ± 2	281 ± 2	324 ± 2	10 ± 1
4Ce	72 ± 3	160 ± 1	250 ± 5	11 ± 2	74 ± 2	192 ± 7	260 ± 10	13 ± 1

The concentrations of Zr and Sc in solid solution were about 0.15 and 0.12%, respectively. Taking into account that Zr and Sc are fully precipitated from the solid solution after annealing, the L_{12} dispersoid volume fraction was estimated as 0.48%. Considering a mean dispersoid size of 10 nm, the maximum Orowan strengthening is approximately 100 MPa.

The alloying with Ce provides a noticeable decrease in the alloy's room temperature strength and an increase in ductility at 4 wt.% Ce. The strength properties degradation can be explained by a formation of the Si and Cu-enriched Ce-bearing phases. As a result, the solute Si in the Ce-bearing alloys decreased and, therefore, the further aging effect due to precipitation of Si and Cu-bearing β'' , β' , Q' phases was weak.

It is notable that a low temperature homogenization provided an increased fraction of Mg_2Si phase of solidification origin and a high number density of the L_{12} $Al_3(Sc,Zr)$ precipitates for Ce-free alloy with a low Sc content. Such a bimodal particle size distribution provided a fine-grained structure and the superplastic behavior with $m \approx 0.4$ and elongation above 300%. At the same time, the Ce-free alloy demonstrated an increased room temperature strength. Alloying with Ce provided a high fraction of the coarse particles that improved the PSN effect, provided grain refinement, and superplasticity. Due to a collaboration of the Zener pinning effect caused by fine L_{12} -dispersoids and PSN effect provided by coarse Ce-bearing particles, the alloys with Ce demonstrated a good superplasticity with $m = 0.42$ and 400–500% of elongation at $(0.2-1) \times 10^{-2} \text{ s}^{-1}$. The disadvantage of the Ce alloying of the studied Al-Mg-Si-Cu based alloys is the dissolution of the precipitation strengthening Si and Cu elements into Ce bearing phase. As a result, Si and Cu content in a solid solution decreased and the aging effect decreased due to the Ce. To improve the strength properties of the Ce bearing Al-Mg-Si-alloys, further chemical composition optimization is required.

4. Conclusions

In this paper, the microstructural evolution, superplastic deformation behavior, and mechanical properties of the Al-Mg-Si-Cu-based alloys containing eutectic forming Ce and dispersoid forming Sc and Zr elements were studied. The main conclusions were drawn as follows:

According to the XRD, SEM, and TEM results, the Al_3CuCe , $\text{Al}_{11}\text{Ce}_3$, and $\text{Al}_{12}\text{Ce}_{10}\text{Si}_8$ phases were solidified in the Ce bearing alloys, and Mg_2Si was formed in the Ce-free and Ce-bearing alloys. The EDS analyses showed that the alloying elements were dissolved into Ce bearing phases; the dissolution of the Si in the Al_3CuCe , Cu in the $\text{Al}_{12}\text{Ce}_{10}\text{Si}_8$ and both Si and Cu in the $\text{Al}_{11}\text{Ce}_3$ phase without the changes of the phases' lattice structure were observed. The increase in the Ce content resulted in an increase in the volume fraction of the Ce-bearing phase particles and a decrease in the volume fraction of the Mg_2Si phase of eutectic origin.

The thermomechanical treatment, including two-step homogenization, with hot and cold rolling, provided a bimodal particle size distribution of the nanoscale L_{12} -structured $\text{Al}_3(\text{Sc,Zr})$ phase precipitates of 10 ± 1 nm size and the coarse particles of eutectic origin. In the Ce-free alloy, the volume fraction of the Mg_2Si particles was 3% and the size was 1.8 ± 0.1 μm . In the Ce-bearing alloys the volume fraction of the Mg_2Si phase was below 0.01. The mean size of the Ce-bearing particles was 1.9 ± 0.1 μm and 1.4 ± 0.1 μm , the volume fraction was 5.5 and 10.5% for alloys with 2% and 4% Ce, respectively.

Due to the pronounced particle stimulated nucleation effect, an increase in the Ce-content improved the superplastic properties, increased the value of elongation-to-failure and decreased flow stress values of the alloys studied. The maximal elongation-to-failure of 500% was achieved at 480 °C and 5×10^{-3} s^{-1} for the alloy with 4% Ce.

The maximal values of the YS and UTS of 367 ± 1 and 420 ± 4 MPa, respectively, were achieved for the Al-Mg-Si-Cu based Ce-free alloy in the T6 state. The Si and Cu dissolution in the Ce-bearing phases weakened the aging effect and led to a significant decrease in strength properties.

Author Contributions: Conceptualization, A.G.M. and A.V.M.; methodology, N.Y.T. and A.S.P.; software, A.G.M.; validation, A.S.P. and A.G.M.; formal analysis, A.S.P.; investigation, A.G.M. and A.V.M.; data curation, A.G.M.; writing—original draft preparation, A.G.M.; writing—review and editing, A.V.M.; visualization, A.G.M.; supervision, A.V.M. All authors have read and agreed to the published version of the manuscript.

Funding: The idea of the study, SEM, EBSD and TEM investigations, mechanical tests were funded by the Russian Science Foundation Grant No. 20-79-00269. The calculations and discussion on the theoretical contribution of the strengthening mechanisms were done in a framework of State Task to Universities of Russian Federation (No. 0718-2020-0030). For TEM studies the equipment of Collective Use Equipment Center “Materials Science and Metallurgy” that works due to financial support of the Russian Federation represented by the Ministry of Higher Education and Science (No. 075-15-2021-696) was used.

Institutional Review Board Statement: Not applicable.

Informed Consent Statement: Not applicable.

Data Availability Statement: The raw and processed data required to reproduce these results are available by contacting the authors.

Conflicts of Interest: The authors declare no conflict of interest.

References

1. Staab, T.E.M.; Krause-Rehberg, R.; Hornauer, U.; Zschech, E. Study of artificial aging in AlMgSi (6061) and AlMgSiCu (6013) alloys by Positron Annihilation. *J. Mater. Sci.* **2006**, *41*, 1059–1066. [[CrossRef](#)]
2. Miller, W.; Zhuang, L.; Bottema, J.; Wittebrood, A.; De Smet, P.; Haszler, A.; Vieregge, A. Recent development in aluminium alloys for the automotive industry. *Mater. Sci. Eng. A* **2000**, *280*, 37–49. [[CrossRef](#)]
3. Heinz, A.; Haszler, A.; Keidel, C.; Moldenhauer, S.; Benedictus, R.; Miller, W. Recent development in aluminium alloys for aerospace applications. *Mater. Sci. Eng. A* **2000**, *280*, 102–107. [[CrossRef](#)]
4. Chakrabarti, D.; Laughlin, D.E. Phase relations and precipitation in Al–Mg–Si alloys with Cu additions. *Prog. Mater. Sci.* **2004**, *49*, 389–410. [[CrossRef](#)]
5. Yang, W.; Wang, M.; Zhang, R.; Zhang, Q.; Sheng, X. The diffraction patterns from β'' precipitates in 12 orientations in Al–Mg–Si alloy. *Scr. Mater.* **2010**, *62*, 705–708. [[CrossRef](#)]

6. Dong, X.; Ji, S. Si poisoning and promotion on the microstructure and mechanical properties of Al–Si–Mg cast alloys. *J. Mater. Sci.* **2018**, *53*, 7778–7792. [[CrossRef](#)]
7. Vissers, R.; van Huis, M.A.; Jansen, J.; Zandbergen, H.W.; Marioara, C.D.; Andersen, S.J. The crystal structure of the β' phase in Al–Mg–Si alloys. *Acta Mater.* **2007**, *55*, 3815–3823. [[CrossRef](#)]
8. Chakrabarti, D.J.; Peng, Y.; Laughlin, D.E. Precipitation in Al–Mg–Si Alloys with Cu Additions and the Role of the Q' and Related Phases. *Mater. Sci. Forum* **2002**, *396–402*, 857–862. [[CrossRef](#)]
9. Miao, W.F.; Laughlin, D.E. Effects of Cu content and preaging on precipitation characteristics in aluminum alloy 6022. *Metall. Mater. Trans. A* **2000**, *31*, 361–371. [[CrossRef](#)]
10. Chauhan, K.P.S. Influence of Heat Treatment on the Mechanical Properties of Aluminium Alloys (6xxx Series): A Literature Review. *Int. J. Eng. Res.* **2017**, *6*, 386–389. [[CrossRef](#)]
11. Sotoudeh, K.; Bate, P.S. Diffusion creep and superplasticity in aluminium alloys. *Acta Mater.* **2010**, *58*, 1909–1920. [[CrossRef](#)]
12. Bobruk, E.V.; Safargalina, Z.A.; Golubev, O.V.; Baykov, D.; Kazykhanov, V.U. The effect of ultrafine-grained states on superplastic behavior of Al–Mg–Si alloy. *Mater. Lett.* **2019**, *255*, 126503. [[CrossRef](#)]
13. Jafarian, H.R.; Mousavi Anijdan, S.H.; Miyamoto, H. Observation of low temperature superplasticity in an ultrafine grained AA6063 alloy. *Mater. Sci. Eng. A* **2020**, *795*, 140015. [[CrossRef](#)]
14. Hussain, M.; Nageswara Rao, P.; Jayaganthan, R. Development of Ultrafine-Grained Al–Mg–Si Alloy Through SPD Processing. *Metallogr. Microstruct. Anal.* **2015**, *4*, 219–228. [[CrossRef](#)]
15. Troeger, L.P.; Starke, E.A. Particle-stimulated nucleation of recrystallization for grain-size control and superplasticity in an Al–Mg–Si–Cu alloy. *Mater. Sci. Eng. A* **2000**, *293*, 19–29. [[CrossRef](#)]
16. Troeger, L.P.; Starke, E.A. Microstructural and mechanical characterization of a superplastic 6xxx aluminum alloy. *Mater. Sci. Eng. A* **2000**, *277*, 102–113. [[CrossRef](#)]
17. Wert, J.A.; Paton, N.E.; Hamilton, C.H.; Mahoney, M.W. Grain refinement in 7075 aluminum by thermomechanical processing. *Metall. Trans. A* **1981**, *12*, 1267–1276. [[CrossRef](#)]
18. Wang, X.; Li, Q.; Wu, R.; Zhang, X.; Ma, L. A Review on Superplastic Formation Behavior of Al Alloys. *Adv. Mater. Sci. Eng.* **2018**, *2018*, 7606140. [[CrossRef](#)]
19. Humphreys, F.J. The nucleation of recrystallization at second phase particles in deformed aluminium. *Acta Metall.* **1977**, *25*, 1323–1344. [[CrossRef](#)]
20. Gutierrez-Urrutia, I.; Muñoz-Morris, M.A.; Morris, D.G. Contribution of microstructural parameters to strengthening in an ultrafine-grained Al–7% Si alloy processed by severe deformation. *Acta Mater.* **2007**, *55*, 1319–1330. [[CrossRef](#)]
21. Rohrer, G.S. Introduction to Grains, Phases, and Interfaces—An Interpretation of Microstructure. *Trans. AIME* 1948, vol. 175, pp. 15–51, by C.S. Smith. *Metall. Mater. Trans. A* **2010**, *41*, 1063–1100. [[CrossRef](#)]
22. Humphreys, F.J. A unified theory of recovery, recrystallization and grain growth, based on the stability and growth of cellular microstructures—I. The basic model. *Acta Mater.* **1997**, *45*, 4231–4240. [[CrossRef](#)]
23. Humphreys, F.J. A unified theory of recovery, recrystallization and grain growth, based on the stability and growth of cellular microstructures—II. The effect of second-phase particles. *Acta Mater.* **1997**, *45*, 5031–5039. [[CrossRef](#)]
24. Manohar, P.A.; Ferry, M.; Chandra, T. Five Decades of the Zener Equation. *ISIJ Int.* **1998**, *38*, 913–924. [[CrossRef](#)]
25. Mikhaylovskaya, A.V.; Mochugovskiy, A.G.; Kotov, A.D.; Yakovtseva, O.A.; Gorshenkov, M.V.; Portnoy, V.K. Superplasticity of clad aluminium alloy. *J. Mater. Process. Technol.* **2017**, *243*, 355–364. [[CrossRef](#)]
26. Portnoy, V.K.; Rylov, D.S.; Levchenko, V.S.; Mikhaylovskaya, A.V. The influence of chromium on the structure and superplasticity of Al–Mg–Mn alloys. *J. Alloys Compd.* **2013**, *581*, 313–317. [[CrossRef](#)]
27. Kotov, A.D.; Mikhaylovskaya, A.V.; Kishchik, M.S.; Tsarkov, A.A.; Aksekov, S.A.; Portnoy, V.K. Superplasticity of high-strength Al-based alloys produced by thermomechanical treatment. *J. Alloys Compd.* **2016**, *688*, 336–344. [[CrossRef](#)]
28. Mikhaylovskaya, A.V.; Kotov, A.D.; Pozdniakov, A.V.; Portnoy, V.K. A high-strength aluminium-based alloy with advanced superplasticity. *J. Alloys Compd.* **2014**, *599*, 139–144. [[CrossRef](#)]
29. Humphreys, J.; Rohrer, G.S.; Rollett, A. Grain Growth Following Recrystallization. In *Recrystallization and Related Annealing Phenomena*; Elsevier: Amsterdam, The Netherlands, 2017; pp. 375–429. ISBN 978-0-08-098235-9.
30. Mochugovskiy, A.G.; Mikhaylovskaya, A.V.; Tabachkova, N.Y.; Portnoy, V.K. The mechanism of L12 phase precipitation, microstructure and tensile properties of Al–Mg–Er–Zr alloy. *Mater. Sci. Eng. A* **2019**, *744*, 195–205. [[CrossRef](#)]
31. Mikhaylovskaya, A.V.; Kishchik, A.A.; Kotov, A.D.; Rofman, O.V.; Tabachkova, N.Y. Precipitation behavior and high strain rate superplasticity in a novel fine-grained aluminum based alloy. *Mater. Sci. Eng. A* **2019**, *760*, 37–46. [[CrossRef](#)]
32. Kishchik, M.S.; Mikhaylovskaya, A.V.; Kotov, A.D.; Drits, A.M.; Portnoy, V.K. Effect of Modes of Heterogenizing Annealing Before Cold Rolling on the Structure and Properties of Sheets from Alloy 1565ch. *Met. Sci. Heat Treat.* **2019**, *61*, 228–233. [[CrossRef](#)]
33. Pozdniakov, A.V.; Barkov, R.Y.; Amer, S.M.; Levchenko, V.S.; Kotov, A.D.; Mikhaylovskaya, A.V. Microstructure, mechanical properties and superplasticity of the Al–Cu–Y–Zr alloy. *Mater. Sci. Eng. A* **2019**, *758*, 28–35. [[CrossRef](#)]
34. Mikhaylovskaya, A.V.; Esmaeili Ghayoumabadi, M.; Mochugovskiy, A.G. Superplasticity and mechanical properties of Al–Mg–Si alloy doped with eutectic-forming Ni and Fe, and dispersoid-forming Sc and Zr elements. *Mater. Sci. Eng. A* **2021**, *817*, 141319. [[CrossRef](#)]
35. Mochugovskiy, A.; Kotov, A.; Esmaeili Ghayoumabadi, M.; Yakovtseva, O.; Mikhaylovskaya, A. A High-Strain-Rate Superplasticity of the Al–Mg–Si–Zr–Sc Alloy with Ni Addition. *Materials* **2021**, *14*, 2028. [[CrossRef](#)] [[PubMed](#)]

36. Murashkin, M.Y.; Sabirov, I.; Medvedev, A.E.; Enikeev, N.A.; Lefebvre, W.; Valiev, R.Z.; Sauvage, X. Mechanical and electrical properties of an ultrafine grained Al–8.5 wt. % RE (RE = 5.4 wt.% Ce, 3.1 wt.% La) alloy processed by severe plastic deformation. *Mater. Des.* **2016**, *90*, 433–442. [[CrossRef](#)]
37. Medvedev, A.E.; Murashkin, M.Y.; Enikeev, N.A.; Valiev, R.Z.; Hodgson, P.D.; Lapovok, R. Enhancement of mechanical and electrical properties of Al-RE alloys by optimizing rare-earth concentration and thermo-mechanical treatment. *J. Alloys Compd.* **2018**, *745*, 696–704. [[CrossRef](#)]
38. Mogucheva, A.; Ziyabkin, D.; Kaibyshev, R. Effect of the Thermomechanical Processing on Microstructure and Properties of an Al-Ce Alloy. *Mater. Sci. Forum* **2012**, *706–709*, 361–366. [[CrossRef](#)]
39. Mikhaylovskaya, A.V.; Kishchik, A.A.; Tabachkova, N.Y.; Kotov, A.D.; Cheverikin, V.V.; Bazlov, A.I. Microstructural Characterization and Tensile Properties of Al-Mg-Fe-Ce Alloy at Room and Elevated Temperatures. *JOM* **2020**, *72*, 1619–1626. [[CrossRef](#)]
40. Stromme, E.T.; Henderson, H.B.; Sims, Z.C.; Kesler, M.S.; Weiss, D.; Ott, R.T.; Meng, F.; Kassoumeh, S.; Evangelista, J.; Begley, G.; et al. Ageless Aluminum-Cerium-Based Alloys in High-Volume Die Casting for Improved Energy Efficiency. *JOM* **2018**, *70*, 866–871. [[CrossRef](#)]
41. Sims, Z.C.; Weiss, D.; McCall, S.K.; McGuire, M.A.; Ott, R.T.; Geer, T.; Rios, O.; Turchi, P.A.E. Cerium-Based, Intermetallic-Strengthened Aluminum Casting Alloy: High-Volume Co-product Development. *JOM* **2016**, *68*, 1940–1947. [[CrossRef](#)]
42. Weiss, D. *High Performance Aluminum Casting Alloys for Engine Applications*; SAE: Warrendale, PA, USA, 2016.
43. Belov, N.A.; Khvan, A.V.; Alabin, A.N. Microstructure and Phase Composition of Al-Ce-Cu Alloys in the Al-Rich Corner. *Mater. Sci. Forum* **2006**, *519–521*, 395–400. [[CrossRef](#)]
44. Belov, N.A.; Naumova, E.A.; Eskin, D.G. Casting alloys of the Al–Ce–Ni system: Microstructural approach to alloy design. *Mater. Sci. Eng. A* **1999**, *271*, 134–142. [[CrossRef](#)]
45. Belov, N.A.; Khvan, A.V. The ternary Al–Ce–Cu phase diagram in the aluminum-rich corner. *Acta Mater.* **2007**, *55*, 5473–5482. [[CrossRef](#)]
46. Gröbner, J.; Mirković, D.; Schmid-Fetzer, R. Thermodynamic aspects of the constitution, grain refining, and solidification enthalpies of Al-Ce-Si alloys. *Metall. Mater. Trans. A* **2004**, *35*, 3349–3362. [[CrossRef](#)]
47. Vončina, M.; Kores, S.; Mrvar, P.; Medved, J. Effect of Ce on solidification and mechanical properties of A360 alloy. *J. Alloys Compd.* **2011**, *509*, 7349–7355. [[CrossRef](#)]
48. Zhang, Z.; Bian, X.; Wang, Y. Microstructural characterization and microhardness of rapidly solidified Al–Ce alloys. *Z. Met.* **2002**, *93*, 578–584. [[CrossRef](#)]
49. Glazoff, M.V.; Khvan, A.V.; Zolotarevsky, V.S.; Belov, N.A.; Dinsdale, A.T. Industrial and Perspective Casting Alloys. In *Casting Aluminum Alloys*; Elsevier: Amsterdam, The Netherlands, 2019; pp. 405–510.
50. Tolley, A.; Radmilovic, V.; Dahmen, U. Segregation in Al₃(Sc,Zr) precipitates in Al–Sc–Zr alloys. *Scr. Mater.* **2005**, *52*, 621–625. [[CrossRef](#)]
51. Fuller, C.; Murray, J.; Seidman, D. Temporal evolution of the nanostructure of Al(Sc,Zr) alloys: Part I—Chemical compositions of Al(ScZr) precipitates. *Acta Mater.* **2005**, *53*, 5401–5413. [[CrossRef](#)]
52. Clouet, E. Excess solvent in precipitates. *Nat. Mater.* **2018**, *17*, 1060–1061. [[CrossRef](#)] [[PubMed](#)]
53. Yakovtseva, O.A.; Sitkina, M.N.; Kotov, A.D.; Rofman, O.V.; Mikhaylovskaya, A.V. Experimental study of the superplastic deformation mechanisms of high-strength aluminum-based alloy. *Mater. Sci. Eng. A* **2020**, *788*, 139639. [[CrossRef](#)]
54. Lee, S.; Utsunomiya, A.; Akamatsu, H.; Neishi, K.; Furukawa, M.; Horita, Z.; Langdon, T. Influence of scandium and zirconium on grain stability and superplastic ductilities in ultrafine-grained Al–Mg alloys. *Acta Mater.* **2002**, *50*, 553–564. [[CrossRef](#)]
55. Kumar, A.; Mukhopadhyay, A.K.; Prasad, K.S. Superplastic behaviour of Al–Zn–Mg–Cu–Zr alloy AA7010 containing Sc. *Mater. Sci. Eng. A* **2010**, *527*, 854–857. [[CrossRef](#)]
56. Avtokratova, E.; Sitdikov, O.; Markushev, M.; Mulyukov, R. Extraordinary high-strain rate superplasticity of severely deformed Al–Mg–Sc–Zr alloy. *Mater. Sci. Eng. A* **2012**, *538*, 386–390. [[CrossRef](#)]
57. Mochugovskiy, A.; Mikhaylovskaya, A.V.; Mufalo, W.; Portnoy, V.K. Superplasticity of Al-Mg-Zr Alloy. *Defect Diffus. Forum* **2018**, *385*, 114–119. [[CrossRef](#)]
58. Mochugovskiy, A.G.; Mikhaylovskaya, A.V.; Zadorognyy, M.Y.; Golovin, I.S. Effect of heat treatment on the grain size control, superplasticity, internal friction, and mechanical properties of zirconium-bearing aluminum-based alloy. *J. Alloys Compd.* **2021**, *856*, 157455. [[CrossRef](#)]
59. Mochugovskiy, A.G.; Mikhaylovskaya, A.V. Comparison of precipitation kinetics and mechanical properties in Zr and Sc-bearing aluminum-based alloys. *Mater. Lett.* **2020**, *275*, 128096. [[CrossRef](#)]
60. Belov, N.A.; Alabin, A.N.; Eskin, D.G.; Istomin-Kastrovskii, V.V. Optimization of hardening of Al–Zr–Sc cast alloys. *J. Mater. Sci.* **2006**, *41*, 5890–5899. [[CrossRef](#)]
61. Seidman, D.N.; Marquis, E.A.; Dunand, D.C. Precipitation strengthening at ambient and elevated temperatures of heat-treatable Al(Sc) alloys. *Acta Mater.* **2002**, *50*, 4021–4035. [[CrossRef](#)]
62. Chao, R.; Guan, X.; Guan, R.; Tie, D.; Lian, C.; Wang, X.; Zhang, J. Effect of Zr and Sc on mechanical properties and electrical conductivities of Al wires. *Trans. Nonferrous Met. Soc. China* **2014**, *24*, 3164–3169. [[CrossRef](#)]
63. Filatov, Y.; Yelagin, V.; Zakharov, V. New Al–Mg–Sc alloys. *Mater. Sci. Eng. A* **2000**, *280*, 97–101. [[CrossRef](#)]
64. Tzeng, Y.-C.; Chung, C.-Y.; Chien, H.-C. Effects of trace amounts of Zr and Sc on the recrystallization behavior and mechanical properties of Al-4.5Zn-1.6Mg alloys. *Mater. Lett.* **2018**, *228*, 270–272. [[CrossRef](#)]

65. He, Y.; Zhang, X.; You, J. Effect of minor Sc and Zr on microstructure and mechanical properties of Al-Zn-Mg-Cu alloy. *Trans. Nonferrous Met. Soc. China* **2006**, *16*, 1228–1235. [[CrossRef](#)]
66. Lityńska-Dobrzyńska, L. Precipitation of Phases in Al-Mg-Si-Cu Alloy with Sc and Zr Additions during Heat Treatment. *Solid State Phenom.* **2007**, *130*, 163–166. [[CrossRef](#)]
67. Dumbre, J.; Kairy, S.K.; Anber, E.; Langan, T.; Taheri, M.L.; Dorin, T.; Birbilis, N. Understanding the formation of (Al,Si)₃Sc and V-phase (AlSc₂Si₂) in Al-Si-Sc alloys via *ex situ* heat treatments and in situ transmission electron microscopy studies. *J. Alloys Compd.* **2021**, *861*, 158511. [[CrossRef](#)]
68. Vo, N.Q.; Dunand, D.C.; Seidman, D.N. Improving aging and creep resistance in a dilute Al-Sc alloy by microalloying with Si, Zr and Er. *Acta Mater.* **2014**, *63*, 73–85. [[CrossRef](#)]
69. Ratchev, P.; Verlinden, B.; Van Houtte, P. Effect of preheat temperature on the orientation relationship of (Mn,Fe)Al₆ precipitates in an AA 5182 Aluminium—Magnesium alloy. *Acta Metall. Mater.* **1995**, *43*, 621–629. [[CrossRef](#)]
70. Esmaeili Ghayoumabadi, M.; Mochugovskiy, A.G.; Tabachkova, N.Y.; Mikhaylovskaya, A.V. The influence of minor additions of Y, Sc and Zr on the microstructural evolution, superplastic behavior, and tensile properties of AA6013 alloy. *J. Alloys Compd.* **2021**, *900*, 163477. [[CrossRef](#)]
71. Pancholi, V.; Kashyap, B. Effect of local strain distribution on concurrent microstructural evolution during superplastic deformation of Al-Li 8090 alloy. *Mater. Sci. Eng. A* **2003**, *351*, 174–182. [[CrossRef](#)]
72. Mukhopadhyay, A.K.; Kumar, A.; Raveendra, S.; Samajdar, I. Development of grain structure during superplastic deformation of an Al-Zn-Mg-Cu-Zr alloy containing Sc. *Scr. Mater.* **2011**, *64*, 386–389. [[CrossRef](#)]
73. Myshlyaev, M.; Mironov, S.; Korznikova, G.; Konkova, T.; Korznikova, E.; Aletdinov, A.; Khalikova, G. EBSD study of superplastically strained Al-Mg-Li alloy. *Mater. Lett.* **2020**, *275*, 128063. [[CrossRef](#)]
74. Brandes, E.A.; Brook, G.B. *Smithells Metals Reference Book*; Elsevier: Amsterdam, The Netherlands, 1992; ISBN 9780080517308.
75. Zener, C.; Hollomon, J.H. Effect of Strain Rate Upon Plastic Flow of Steel. *J. Appl. Phys.* **1944**, *15*, 22–32. [[CrossRef](#)]
76. Sellars, C.M.; McTegart, W.J. On the mechanism of hot deformation. *Acta Metall.* **1966**, *14*, 1136–1138. [[CrossRef](#)]
77. Chen, L.; Zhao, G.; Yu, J.; Zhang, W. Constitutive analysis of homogenized 7005 aluminum alloy at evaluated temperature for extrusion process. *Mater. Des.* **2015**, *66*, 129–136. [[CrossRef](#)]
78. Yang, J.; Wu, J.; Zhang, Q.; Han, R.; Wang, K. The simple hyperbolic-sine equation for superplastic deformation and parameters optimization. *J. Mater. Res. Technol.* **2020**, *9*, 10819–10829. [[CrossRef](#)]
79. Ruano, O.A.; Sherby, O.D. On constitutive equations for various diffusion-controlled creep mechanisms. *Rev. Phys. Appl.* **1988**, *23*, 625–637. [[CrossRef](#)]
80. Kawasaki, M.; Balasubramanian, N.; Langdon, T.G. Flow mechanisms in ultrafine-grained metals with an emphasis on superplasticity. *Mater. Sci. Eng. A* **2011**, *528*, 6624–6629. [[CrossRef](#)]
81. Kotov, A.D.; Mikhaylovskaya, A.V.; Portnoy, V.K. Effect of the solid-solution composition on the superplasticity characteristics of Al-Zn-Mg-Cu-Ni-Zr Alloys. *Phys. Met. Metallogr.* **2014**, *115*, 730–735. [[CrossRef](#)]
82. Kaneko, R.S.; Bakow, L.; Lee, E.W. Aluminum alloy 6013 sheet for new U.S. Navy aircraft. *JOM* **1990**, *42*, 16–18. [[CrossRef](#)]